Theory of viscoelastic lubrication

M. Scaraggi [a,b,*], B.N.J. Persson [b]

[a] DII, Universitá del Salento, 73100 Monteroni-Lecce, Italy
[b] Peter Grünberg Institut-1, FZ-Jülich, 52425 Jülich, Germany

ARTICLE INFO

ABSTRACT

We study the lubricated (wet) contact mechanics of a smooth hard cylinder sliding on a randomly rough nominally flat surface of a linear viscoelastic solid. We calculate the rolling and sliding friction, and study the transition from the boundary lubrication to the elasto-hydrodynamic lubrication regime. For the viscoelastic contact the minimum (average) separation does not monotonically increase with the sliding velocity, and the Stribeck curve exhibits new structures not shown for elastic solids.

© 2013 Elsevier Ltd. All rights reserved.

1. Introduction

Wet rubber friction is a topic of huge practical importance. It involves contact mechanics between rough surfaces, and polymer dynamics of compliant bodies, and it occurs in a remarkably wide range of applications such as tire-road contact [1], rubber sealing [2,3] and wiper blades contacts [4], in the mechanics of biological interfaces [5,6] and, consequently, of bio-inspired (e.g. adhesives [7]) and bio-medical devices (e.g. prosthesis [8], scaffolds [9], and gliding devices [10]).

Studies of friction involving viscoelastic solids have mainly focused on the investigation of dry contacts [11–14]. Rolling friction experiments for smooth surfaces are usually performed with a hard cylinder or sphere rolling on a flat rubber substrate [14–17]. However, sliding friction experiments will give nearly the same friction if the interface is (almost) shear stress free, e.g. for lubricated surfaces where the fluid film has a thickness much smaller than the rigid penetration of the ball, but larger than the amplitude of the surface roughness [14].

Most analytical theories of rubber rolling friction are based on a simplified description of the rubber rheology [12,13], i.e. on a single term Prony series. However, the relaxation spectrum of real polymers is usually very wide and the rolling friction of real rubber compounds cannot be predicted using those exact theories. Therefore, rolling friction experiments have so far been analyzed mainly using the well known Greenwood and Tabor formula [14],

which relies on an unknown α-factor determined by the viscoelastic hysteretic behavior of the rubber.

Recently, one of us (BNJP) has developed a Fourier-space based approach for the prediction of rolling friction for real rubber materials [11]. This approach, accurate to linear order in the loss tangent, is able to predict quantitatively reliable results, as shown for both line [11] (see also in the following) and point contacts [18], with negligible computational effort. Unfortunately, the latter approach does not allow to determine the traction and the displacement fields occurring at the contact.

Full numerical solutions of the viscoelastic contact problem, of interest for many tribological applications, have only very recently been presented for smooth and rough contacts, see e.g. Ref. [18]. This should not surprise at all, due to the numerical complexity of the underlying problem, which is even more pronounced in case of real (multiscale) rough contacting surfaces. As a result, the hysteretic rubber friction coming from local sliding contacts can be, nowadays, only effectively calculated using homogenized contact mechanics theories [19].

Despite the huge number of practical applications, the role of viscoelasticity in the contact mechanics of wet interacting real solids has not been studied theoretically to the same extent as for dry contact. Very interesting pioneering works on viscoelasticity and lubrication have been presented by Hooke and Huang [20], and by Elsharkawy [21]. These authors consider the influence of rubber hysteresis on lubricated contacts in the hydrodynamic regime. For steady sliding contacts they highlight the role of the viscoelasticity retardation process on the generation of a peculiar asymmetric fluid pressure field, a feature which will be also shown in the following. However, we are not aware of a (even qualitative) study of the influence of viscoelasticity on the Stribeck curve for

---

Nomenclature

$C(\mathbf{q})$	roughness power spectral density (m^4)
D_f	fractal dimension for the case of self-affine roughness
$E(\omega)$	rubber complex elastic modulus (Pa)
E_0	relaxed (i.e. low frequency) rubber elastic modulus (Pa)
E_∞	stiff (i.e. high frequency) rubber elastic modulus (Pa)
E_{r0}	relaxed (i.e. low frequency) reduced rubber elastic modulus, $E_{r0} = E_0/(1-\nu^2)$ (Pa)
$E_{r\infty}$	stiff (i.e. high frequency) reduced rubber elastic modulus, $E_{r\infty} = E_\infty/(1-\nu^2)$ (Pa)
$E_r(\omega)$	reduced rubber complex elastic modulus, $E_r(\omega) = E(\omega)/(1-\nu^2)$ (Pa)
F_N	normal load, applied on a cylinder length L (N)
$J(t)$	rubber creep function (Pa^{-1})
$L(t)$	rubber spectral density [(Pa s)$^{-1}$]
R	cylinder radius (m)
$\Gamma(t)$	$\Gamma(t) = E(\infty)\int_0^\infty d\tau[L(\tau)/\tau]e^{-t/\tau}$ (s^{-1})
η	fluid viscosity (Pa s)
η_0	low shear fluid viscosity (Pa s)
$\mathbf{v}_0$	sliding velocity (m/s)
σ_s	frictional shear stress in the real contact area (Pa)
$\tilde{J}(\omega)$	rubber complex creep function $\tilde{J}(\omega) = 1/E(\omega)$ (Pa^{-1})
f_N	line normal load (N/m)
$f_{shape}(x)$	rigid cylinder profile (m)
h_{rms}	root-mean-square roughness (m)
q_0	small wavelength cut-off (m^{-1})
q_1	large wavelength cut-off (m^{-1})
Q	rolling number

μ	friction
μ_{Rc}	solid contact rolling friction
μ_{Rf}	wet rolling friction
μ_{Sc}	solid contact sliding friction
μ_{Sf}	wet sliding friction
a_0	Hertzian semicontact length calculated with the relaxed (i.e. low frequency) rubber elastic modulus E_0 (m)
p_0	Hertzian maximum pressure calculated with the relaxed (i.e. low frequency) rubber elastic modulus E_0 (Pa)
u_{min}	minimum (locally averaged) interfacial separation (m)
$A/A_0(x)$	normalized real contact area
$J(x)$	mean field fluid flow (m^2/s)
$\boldsymbol{\tau}(x)$	$\boldsymbol{\tau} = \boldsymbol{\tau}_f + \boldsymbol{\tau}_c$ (Pa)
$\boldsymbol{\tau}_c(x)$	mean field wall shear stress coming from solid contact (Pa)
$\boldsymbol{\tau}_f(x)$	mean field wall shear stress coming from fluid action (Pa)
$\mathbf{v}(\mathbf{x})$	fluid velocity (m/s)
$\mathbf{x}$	generic position $\mathbf{x} = (x,y)$ in the contact domain (m)
$\phi_{fp}(x)$	(tensorial) pressure friction factor
$\phi_f(x)$ and $\phi_{fs}(x)$	(tensorial) shear friction factors
$\phi_p(x)$	(tensorial) pressure flow factor
$\phi_s(x)$	(tensorial) shear flow factor
$p_0(x)$	$p_0 = p_c + p_f$ (Pa)
$p_c(x)$	mean field contact pressure (Pa)
$p_f(x)$	mean field fluid pressure (Pa)
$u(x)$	mean field interfacial separation (m)
$u_z(x)$	mean field surface (out-of-plane) displacement (m)

the whole range of sliding speeds. In this paper we give our first contribution to this topic, and in particular by studying *the effects of viscoelasticity and random surface height fluctuations on the Stribeck curve*, as well as on the traction and separation fields occurring at the contact interface of steady sliding line contacts. It will be shown, for the first time, how the solid bulk hysteresis influences the mixed lubrication by varying the lubrication conditions of a generic contact.

We introduce the *rolling number* $Q = v_{GT}/v_{ML}$, where v_{ML} is a typical sliding velocity in the mixed lubrication (ML) region, and v_{GT} a typical velocity in the transition region from rubbery to glassy response of the rubber (named glassy transition in what follows). The latter can also be defined as the velocity determined by $v \approx \tilde{\omega} \, w(\tilde{\omega})$, where $\tilde{\omega}$ is the frequency where the loss tangent $\tan\delta(\omega)$ is maximal, and where $w(\tilde{\omega})$ is the width of the nominal cylinder-substrate contact region. For $Q \ll 1$ the dissipation originating from the rubber hysteresis will occur in the boundary lubrication regime, whereas for $Q \gg 1$ the viscoelastic dissipation will superpose to the wet sliding friction in the hydrodynamic regime. The full Stribeck curve, including all sources of energy dissipation, will also be calculated for real rubber materials.

The paper is organized as follows. In Section 2 the wet viscoelastic contact mechanics model is presented and discussed, whilst a comparison with existing results is reported in Section 3.1. In Section 3.2, for a viscoelastic solid with simple rheology, the investigation focuses on the combined effect of the rubber-to-glass transition and mixed-lubrication transition on the Stribeck curve and on the mean fields describing the contact. Finally, in Section 4 the rolling friction is discussed for real rubber materials, for which a correct rheological description is required in order to obtain accurate friction predictions. In the Appendix A–D the details about the numerical model, as well as a brief introduction on the

role of viscoelasticity in the fluid-induced asperities flattening, are reported.

2. Mean field theory for randomly rough wet viscoelastic contact

We now develop a mean-field theory for the lubricated contact of viscoelastic solids with randomly rough surfaces. The fluid is assumed to be Newtonian, and operating in isothermal and isoviscous conditions. The geometry is shown in Fig. 1 (line-contact case).

Consider a rigid cylinder with a perfectly smooth surface in relative sliding motion with respect to an isotropic viscoelastic half space with a randomly rough surface. At the macroscopic level a steady state prevails. Assuming a large separation of length scales between the width of the (apparent) cylinder-substrate Hertz's contact region and the wavelength of the longest relevant surface roughness component, a steady state will to a good approximation
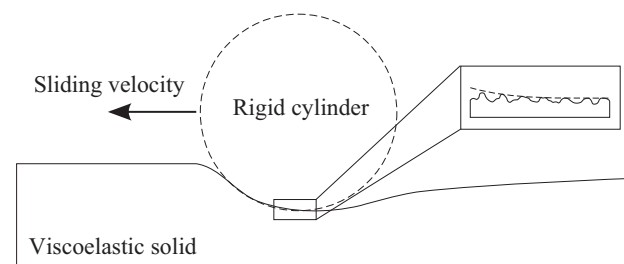

Fig. 1. A smooth rigid cylinder in steady sliding contact with a randomly rough viscoelastic counterpart (schematic).

prevail also at the roughness length scale. As shown in the magnification insert of Fig. 1, at the roughness length scale the contact (between the cylinder and the substrate) will be partial in the most general case and, in particular, this will strictly depend on the actual lubrication regime. The exact local contact condition can be easily calculated within the model developed in the following, which describes the transition from the boundary to the visco-elastohydrodynamic lubrication regime.

Consider the fluid flow at the interface between the solids. The fluid velocity field $\mathbf{v}(\mathbf{x}, t)$ is assumed to satisfy the Navier–Stokes equation, and the fluid to be incompressible, i.e. $\nabla \cdot \mathbf{v} = 0$. Neglecting the non-linear term $\mathbf{v} \cdot \nabla \mathbf{v}$ in the momentum equation, which is usually a good approximation for the fluid flow between narrowly spaced solid walls, the Navier–Stokes equation can be simplified to

$$\eta \frac{\partial^2 \mathbf{v}}{\partial z^2} = \nabla p, \tag{1}$$

where η is the fluid viscosity and p the fluid pressure. At the smallest roughness length scales the Newtonian-fluid assumption is not expected to hold due to the nanometer sized average surface separations, and the resulting high shear rates. However, this aspect can be easily taken into account in the homogenized fluid formulation [22–25], which is briefly summarized in the following.

One way to integrate out the surface roughness in Eq. (1) is by using the renormalization-group procedure, see Ref. [23] for the theory. In this procedure one eliminates or integrates out the surface roughness components in steps and obtains a set of renormalization-group flow equations describing how the effective fluid equation evolves as more and more of the surface roughness components are eliminated. One can show that, after eliminating all the surface roughness components, the average fluid flow obeys the following equation [23]:

$$\mathbf{J} = -\frac{u^3 \phi_{\mathrm{p}}(u)}{12\eta_0} \nabla p_{\mathrm{f}} + \frac{1}{2} u \mathbf{v}_0 + \frac{1}{2} h_{\mathrm{rms}} \phi_{\mathrm{s}}(u) \mathbf{v}_0, \tag{2}$$

where the pressure flow factor ϕ_{p} and the shear flow factor ϕ_{s} (for anisotropic surface roughness) are 2×2 matrices. η_0 is the low shear-rate viscosity, $u = u(\mathbf{x})$ and $p_{\mathrm{f}} = p_{\mathrm{f}}(\mathbf{x})$ are, respectively, the (locally averaged) interfacial separation and fluid pressure, h_{rms} is the rubber root mean square roughness, and $\mathbf{v}_0$ is the cylinder sliding velocity. Mass conservation demands that

$$\nabla \cdot \mathbf{J} = 0. \tag{3}$$

The locally averaged (cylinder) wall shear stress $\boldsymbol{\tau} = (\tau_{zx}, \tau_{zy})$ is the sum $\boldsymbol{\tau} = \boldsymbol{\tau}_{\mathrm{f}} + \boldsymbol{\tau}_{\mathrm{c}}$ of a fluid contribution $\boldsymbol{\tau}_{\mathrm{f}}$, and a contribution from the area of contact $\boldsymbol{\tau}_{\mathrm{c}}$ [23]:

$$\boldsymbol{\tau}_{\mathrm{f}} = -(\phi_{\mathrm{f}} + \phi_{\mathrm{fs}}) \frac{\eta_0 \mathbf{v}_0}{u} - \phi_{\mathrm{fp}} \frac{1}{2} u \nabla p_{\mathrm{f}}, \tag{4}$$

$$\boldsymbol{\tau}_{\mathrm{c}} = -\frac{\mathbf{v}_0}{|\mathbf{v}_0|} \frac{A}{A_0} \sigma_{\mathrm{s}}, \tag{5}$$

where ϕ_{f}, ϕ_{fs} and ϕ_{fp} are frictional correction factors [23], σ_{s} is the frictional shear stress in the real solid contact areas A. Due to the (approximately) steady-state contact condition occurring at the roughness length scale, the flow as well as the frictional correction factors, entering in Eqs. (2) and (4), are similar to those developed in Ref. [23] for the elastic solid bulk rheology, with the only difference that in this case the rubber elastic modulus, which enters in the correction factors calculation through the Persson's contact mechanics [19], is varying with the sliding velocity (see later).

In the most general case, the (real) contact shear stress σ_{s} [entering in Eq. (5)] depends on the local (asperity-scale) contact condition, i.e. on the local boundary state. Recent studies have shown that for a wetting liquid (positive spreading pressure S) an

ordered packaging of few lubricant monolayers [26,27] (of nanometers sized gap) with almost solid-like properties may form in the contact regions. In such a case, the shear stress can be nearly proportional to the logarithm of sliding velocity for low sliding velocity (of order 10 µm/s, or even larger), as a consequence of thermal activation [28]. However, in the well studied case of hydrocarbons lubrication [27], the relation between the sliding velocity and shear stress can be quite complex, and will depend on the exact number of trapped (in the asperity contact regions) lubricant monolayers [26,27].

For simple fluids and locally smooth contacts, if the spreading pressure S is negative, below a critical sliding velocity V_{d} a dewetting transition will occur (i.e. leading to a dry asperity contact). V_{d} is approximately given by [29][1]

$$V_{\mathrm{d}} 2em = \frac{k|S^2|}{\eta\, Ee}, \tag{6}$$

where k is a prefactor of order one, η is the lubricant bulk viscosity, E the elastic modulus and S the spreading pressure, given by $S = \gamma_{\mathrm{SR}} - (\gamma_{\mathrm{SL}} + \gamma_{\mathrm{LR}})$ [S compares the interfacial energies between dry (γ_{SR}) and lubricated ($\gamma_{\mathrm{SL}} + \gamma_{\mathrm{LR}}$) contact conditions, e.g. $S < 0$ for a dewetting contact]. The smallest local (asperity-scale) separation is denoted by e, and may be the width of a single lubricant monolayer, but is usually larger. If $v_0 < V_{\mathrm{d}}$ the contact regions will preferentially occur in a dry state, but nucleation of dewetting is often a thermally activated process, and will involve some activation time which depends on the energetic barriers involved (which depends on the fluid film thickness). If the contact regions are in the dry state the effective shear stress will be the sum of three contributions [10]: $\sigma_{\mathrm{s}} = \sigma_{\mathrm{s}1} + \sigma_{\mathrm{s}2} + \sigma_{\mathrm{s}3}$. Here $\sigma_{\mathrm{s}1}$ corresponds to the shear stress coming from the breaking of (usually) weak bonds (e.g. van der Waals or hydrogen bonds) formed by the rubber binding to the hard substrate [30,31], $\sigma_{\mathrm{s}2}$ is the shear stress related to the energy dissipation in the crack opening processes occurring at the edge of the contacting regions, whereas $\sigma_{\mathrm{s}3}$ is related to the energy dissipation originating from the pulsating indentations of the rubber by the hard asperities of the counter surface (the latter mechanism is absent in the contact configuration we study, where the counter-surface is assumed perfectly smooth). In this work σ_{s} is considered constant but our findings are not expected to be qualitatively affected by the correct description of σ_{s}. Finally, note that the speed of dewetting may depend on the viscoelastic hysteresis which was not included in deriving Eq. (6). However the major limitation to the application of Eq. (6) is the multiscale nature of the surface roughness which exists on almost all real surfaces, and the lack of physical modeling of the collective dynamics of dewetting asperities, whose long-ranged interactions are due to both the (visco-) elasticity of the solids and the fluid flow conservation constraint. Unfortunately a model for such dewetting dynamics has not been presented in the literature.

In this work, the (locally averaged) asperities interactions, originating from the rubber bulk deformation, are described within the Persson's contact mechanics theory [19,32–34]. Observe that, in the adopted contact configuration, the substrate asperities (at all length scales) in the cylinder-substrate contact region undergo pulsating deformations characterized by the deformation frequency $\omega_{\mathrm{H}} \approx \pi v_0 / a_{\mathrm{H}}$, where $a_{\mathrm{H}}^2 = 4 f_{\mathrm{N}} R / (\pi |E_{\mathrm{r}}(\omega_{\mathrm{H}})|)$, with $f_{\mathrm{N}} = F_{\mathrm{N}}/L$ the line load (force per unit length), R the cylinder radius and $E_{\mathrm{r}}(\omega_{\mathrm{H}})$ the complex reduced elastic modulus [$E_{\mathrm{r}}(\omega_{\mathrm{H}}) = E(\omega_{\mathrm{H}})/(1 - \nu^2)$], where $E(\omega_{\mathrm{H}})$ is the complex Young's modulus (at frequency ω_{H}) and ν is the Poisson ratio (assumed independent of frequency, see also in the

---

[1] A critical sliding velocity, describing the transition between a wetted and a dewetted state, can be determined by balancing the flow expelled from the junction, as induced by the spreading pressure S, to the forced wetting flow introduced by the sliding action [29].

following). If the cylinder would exhibit surface roughness too, a more complex theory would be required, which will be the subject of a companion contribution.

The contact mechanics formalism of Persson is based on studying the interface between two contacting solids at different magnification ζ. When the system is studied at the magnification ζ it appears as if the contact area (projected on the xy-plane) equals $A(\zeta)$, but when the magnification increases it is observed that the contact is effectively incomplete, and the surfaces in the apparent contact area $A(\zeta)$ are in fact separated by the average distance $u(\zeta)$. Within this formalism, the real normalized contact area A/A_0 is given by [19,32–34]

$$\frac{A(\mathbf{x})}{A_0} = \frac{1}{(\pi G)^{1/2}} \int_0^{p_c(\mathbf{x})} d\sigma \ e^{-\sigma^2/(4G)} = \text{erf}\left[\frac{p_c(\mathbf{x})}{2G^{1/2}}\right], \tag{7}$$

with

$$G = \frac{1}{8}|E_r(\omega_H)|^2 \int_{q_0 \leq |\mathbf{q}| \leq q_1} d^2q \ q^2 C(\mathbf{q}),$$

where q_0 and q_1 are, respectively, a low and high roughness frequency cut-offs, and where the surface roughness power spectrum:

$$C(\mathbf{q}) = \frac{1}{(2\pi)^2} \int d^2x \langle h(\mathbf{x})h(\mathbf{0}) \rangle e^{-i\mathbf{q} \cdot \mathbf{x}},$$

where $h(\mathbf{x})$ is the surface roughness profile, with $\langle h(\mathbf{x}) \rangle = 0$. Here $\langle \cdots \rangle$ stands for an ensemble average and $p_c = p_c(\mathbf{x})$ is the (locally averaged) solid contact pressure. The average interfacial separation $u(\mathbf{x})$ can be calculated from [34]

$$u(\mathbf{x}) = \sqrt{\pi} \int_{q_0}^{q_1} dq \ q^2 C_{avg}(q)w(q) \times \int_{p_c(\mathbf{x})/|E_r(\omega_H)|}^{\infty} dp' \frac{1}{p'} e^{-[w(q)p']^2}, \tag{8}$$

where

$$w(q) = \left(\pi \int_{q_0}^{q} dq' \ q'^3 C_{avg}(q')\right)^{-1/2}$$

and $C_{avg}(q = |\mathbf{q}|) = \langle C(\mathbf{q}) \rangle_\theta$, with $\langle \rangle_\theta$ the angular average operator.

In order to determine the locally averaged surface deformation of the viscoelastic half space, we assume that the quasi-static bulk dynamics holds, i.e. inertia effects are neglected. If a stress $\sigma_z(\mathbf{x}, t)$ acts on the surface of a semi-infinite viscoelastic solid it will result in a normal surface displacement $u_z(\mathbf{x}, t)$ which is linearly related to $\sigma_z(\mathbf{x}, t)$ via an equation which is particularly simple when the spatial and time coordinates are Fourier transformed [19]:

$$u_z(\mathbf{q}, \omega) = M_{zz}(\mathbf{q}, \omega)\sigma_z(\mathbf{q}, \omega), \tag{9}$$

where

$$M_{zz}(\mathbf{q}, \omega) = -\frac{2(1-\nu^2)}{qE(\omega)}. \tag{10}$$

In this work the Poisson ratio $\nu(\omega)$ is assumed independent of frequency. This assumption is a good approximation in most cases (see e.g. Ref. [11]), and it means that the dynamics of relaxation in orthogonal directions proceeds equally in time. If a rigid cylinder is sliding in steady state on a semi-infinite rubber solid we have

$$\sigma_z(\mathbf{x}, t) = \sigma_z(\mathbf{x} - \mathbf{v}t),$$

which gives

$$\sigma_z(\mathbf{q}, \omega) = \delta(\mathbf{q} \cdot \mathbf{v} - \omega)\sigma_z(\mathbf{q}). \tag{11}$$

For the cylinder geometry with the cylinder axis along the y-direction, $\sigma_z(\mathbf{x})$ is independent of y and we write $\sigma_z(\mathbf{x}) = -p(x)$ so that

$$\sigma_z(\mathbf{q}) = -p(q_x)\delta(q_y). \tag{12}$$

Using Eqs. (9)–(12) gives

$$u_z(\mathbf{q}, \omega) = \frac{2(1-\nu^2)}{|q_x|E(\omega)}p(q_x)\delta(q_y)\delta(q_x v_x - \omega).$$

Thus we get

$$u_z(x, t) = \int d^2q \ d\omega \ u_z(\mathbf{q}, \omega)e^{i(\mathbf{q} \cdot \mathbf{x} - \omega t)}$$
$$= \int d\omega \frac{2(1-\nu^2)}{|\omega|E(\omega)}p(\omega/v_x)e^{i\omega(x/v_x - t)}. \tag{13}$$

Now because of causality one can write

$$\frac{1}{E(\omega)} = \frac{1}{E(\infty)} + \int_0^\infty d\tau \frac{L(\tau)}{1 - i\omega\tau}, \tag{14}$$

where $L(\tau)$ is the spectral density and τ a rubber relaxation time. Note that we can also write

$$\frac{1}{E(\omega)} = \frac{1}{E(\infty)}\left[1 + \int_0^\infty dt \ \Gamma(t)e^{i\omega t}\right], \tag{15}$$

where

$$\Gamma(t) = E(\infty) \int_0^\infty d\tau \frac{L(\tau)}{\tau}e^{-t/\tau}.$$

We write

$$p(q_x) = \frac{1}{2\pi} \int dx' \ p(x')e^{-iq_x x'}. \tag{16}$$

Substituting (15) and (16) in (13) gives

$$u_z(x, t) = \frac{(1-\nu^2)}{\pi E(\infty)} \int dx' \int d\omega \frac{1}{|\omega|}p(x')$$
$$\times \left[e^{i\alpha\omega/v_x} + \int_0^t dt' \ \Gamma(t')e^{i\beta(t')\omega/v_x}\right], \tag{17}$$

where $\alpha = x - x' - v_x t$ and $\beta(t') = x - x' - v_x(t - t')$. Now consider the integral:

$$I = \int_{-\infty}^\infty d\omega \frac{1}{|\omega|}e^{i\alpha\omega/v_x}.$$

We write $\omega/v_x = q_x$ and get

$$I = 2 \int_0^\infty dq_x \frac{\cos(\alpha q_x)}{q_x}.$$

This integral diverges. The problem arises from the small wave-vector region $q_x \to 0$ and, as well known, reflects the infinite size of the system. For a finite (but very large) solid with linear dimension L we must replace the lower integration limit with π/L so that

$$I = 2 \int_{\pi/L}^\infty dq_x \frac{\cos(\alpha q_x)}{q_x}.$$

Let us denote $|\alpha|q_x = \xi$ so that

$$I = 2 \int_{|\alpha|\pi/L}^\infty d\xi \frac{\cos\xi}{\xi}.$$

For large (but fixed) L this will give

$$I \approx \text{const.} - 2\log|\alpha|.$$

Using this result in Eq. (17) gives

$$u_z(x, t) = \text{const.} - \frac{2(1-\nu^2)}{\pi E(\infty)} \int dx' \ p(x')$$
$$\times \left[\log|x - x' - v_x t| + \int_0^t dt' \ \Gamma(t')\log|x - x' - v_x(t - t')|\right]. \tag{18}$$

In what follows we study the system in a coordinate system fixed in the cylinder which corresponds to replacing $x \to x + v_x t$, with $v_x = v_0$. We also denote the high-frequency modulus $E(\infty)$ with E_∞, and the low-frequency modulus $E(0)$ with E_0. We consider long
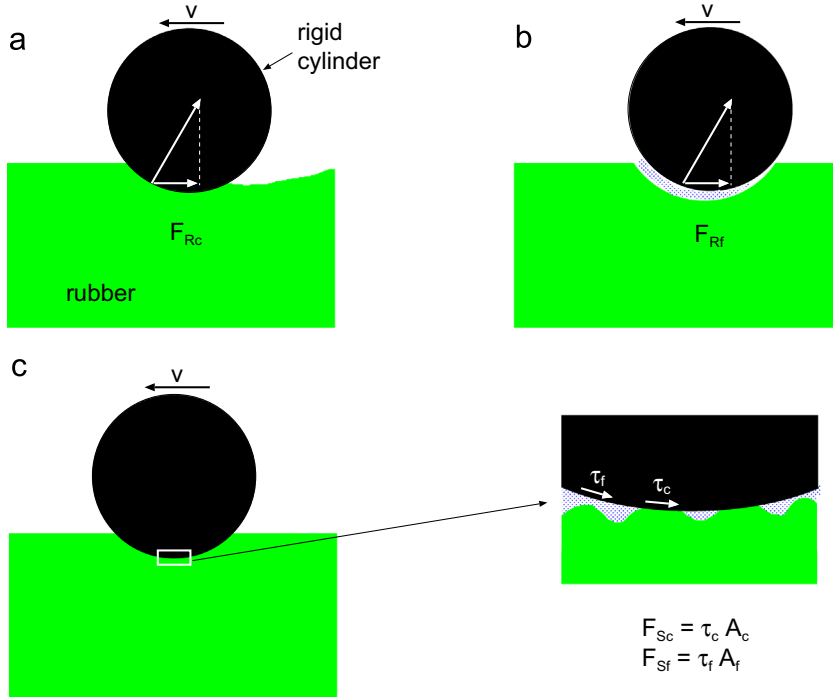
Fig. 2. Friction sources at the sliding contact interface (schematic). (a) The solid contact rolling friction contribution corresponds to the projection on the sliding plane of the resultant of the (locally averaged) solid contact pressure acting on the cylinder. It arises from the rubber deformation losses. (b) The wet rolling friction contribution corresponds to the projection on the sliding plane of the resultant of the (locally averaged) fluid pressure acting on the cylinder. Depending on the rolling number Q, it may arise mainly from the rubber deformation losses or from the fluid viscous losses. (c) The third friction contribution comes from the shear stresses (τ_f and τ_c) acting on the cylinder wall from the fluid or the asperity contact regions.

times $t \to \infty$ where the sliding is steady state, where $u(x, t) = u(x)$ (in the moving reference frame) is time independent. With these assumptions, and denoting the pressure $p(x)$ by $p_0(x)$, we get

$$u_z(x) = \text{const.} - \frac{2(1-\nu^2)}{\pi E_\infty} \int dx' \, p_0(x')$$
$$\times \left[\log|x-x'| + \int_0^\infty dt' \, \Gamma(t') \log|x-x'+v_0 t'|. \right] \quad (19)$$

The derivation above is for a homogeneous viscoelastic half-space, but can be easily generalized to a layered material, which just introduce in (10) an additional factor $S(q, \omega)$ which is known analytically (see e.g., Ref. [35]). The viscoelastic deformation equation links the average pressure $p_0(x)$ to the average interfacial separation. For a cylinder contact we have, finally:

$$u(x) = u_0 + \frac{x^2}{2R} - \frac{2}{\pi E_{r\infty}} \int_{-\infty}^\infty dx' \, p_0(x') \frac{\log|x-x'|}{\log|x'|}$$
$$- \frac{2}{\pi E_{r\infty}} \int_{-\infty}^\infty dx' \, p_0(x') \int_0^\infty dt \, \Gamma(t) \frac{\log|x-x'+tv_0|}{\log|-x'+tv_0|}, \quad (20)$$

where $E_{r\infty} = E_\infty/(1-\nu^2)$ and where u_0 is the average central separation [i.e. $u_0 = u(x=0)$] and $p_0(x) = p_f(x) + p_c(x)$. u_0 can be implicitly calculated with the load balance equation:

$$\int_{-\infty}^\infty dx' \, p_0(x') = f_N, \quad (21)$$

where $f_N = F_N/L$ is the cylinder load per unit length, as before. Eqs. (3), (7), (8), (20), and (21) have to be solved to determine the unknown variables p_f, p_c, u and u_0. In the theory presented above, cavitation is assumed to occur only on the macroscopic scale.

Finally, the total friction coefficient μ, related to the friction force acting on the rigid cylinder, is the sum of four contributions in the adopted contact condition (see Fig. 2), i.e.:

$$\mu = \mu_{Rc} + \mu_{Rf} + \mu_{Sc} + \mu_{Sf},$$

where the solid contact rolling friction μ_{Rc} and the wet rolling friction μ_{Rf} can be calculated, respectively, from

$$\mu_{Rc} = -\frac{1}{f_N} \int dx \, p_c(x) f_{shape}'(x)$$

$$\mu_{Rf} = -\frac{1}{f_N} \int dx \, p_f(x) f_{shape}'(x),$$

and where the solid contact sliding friction μ_{Sc} and the wet sliding friction μ_{Sf} can be calculated, respectively, from

$$\mu_{Sc} = \frac{1}{f_N} \int dx \, \tau_c$$

$$\mu_{Sf} = \frac{1}{f_N} \int dx \, \tau_f.$$

$f_{shape}(x)$ corresponds to the rigid cylinder profile, i.e. $x^2/(2R)$ in the parabolic assumption.

3. Numerical results: model rubber

3.1. Dry rolling friction: role of surface roughness

We first study rolling friction in the case of negligible fluid (viscous) effect, i.e. in the boundary or dry lubrication regime. In this case the solid contact rolling friction results obtained using our theory can be compared to the predictions for smooth surfaces presented by one of us [11].

Consider a rigid smooth cylinder in sliding (or rolling) contact with a randomly rough viscoelastic half-space characterized by a single relaxation time, with $E_\infty/E_2 = 9$ (see Appendix B) and with relaxation time τ_r. The rough surface has isotropic, self-affine fractal roughness with fractal dimension $D_f = 2.2$, small wavevector cut-off $q_0 = 2 \times 10^5$ m^{-1}, high wavevector cut-off $q_1 = 7.8 \times 10^9$ m^{-1}, and the root-mean-square roughness
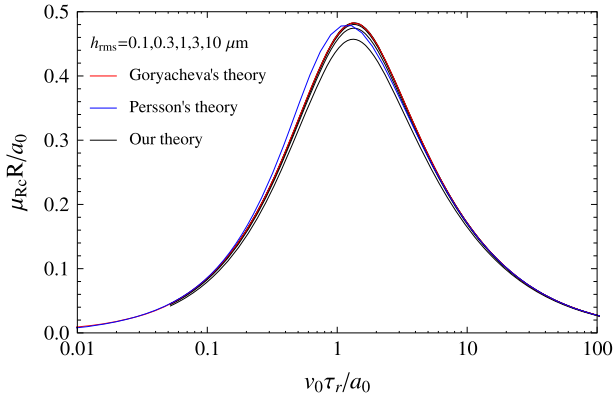
Fig. 3. (Colour online) Dry rolling friction as a function of the dimensionless sliding velocity $v_0\tau_r/a_0$ for different values of root-mean-square roughness (black curves). The blue curve is calculated with the theory developed in Ref. [11], and the red curve is the exact rolling friction for smooth cylinder contact [12,13]. For $E_\infty/E_0 = 10$.
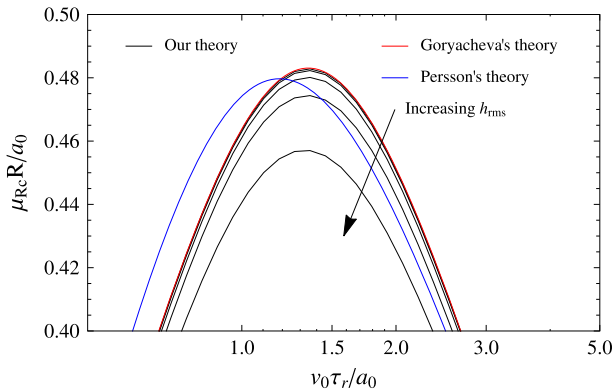

Fig. 4. (Colour online) Magnification of the highest friction region of Fig. 3. Observe that increasing the roughness magnitude reduces the maximum rolling friction.

$h_{rms} = \langle h^2 \rangle^{1/2} = 0.1, 0.3, 1, 3, 10 \, \mu m$ (with $\langle h \rangle = 0$). The frictional shear stress in the area of real contact is assumed to vanish. Fig. 3 shows μ_{Rc} as a function of the dimensionless sliding velocity $v_0\tau_r/a_0$, where a_0 is the calculated (Hertzian) half-width of the contact strip, obtained using the relaxed elastic modulus E_0. Results are shown for different values of root-mean-square roughness (black curves). The blue curve is calculated with the theory developed in Ref. [11], and the red curve is the exact rolling friction for cylinder contact [12,13] (both theories assume perfectly smooth surfaces).

Observe that the maximum value of the rolling friction decreases with increasing roughness, Fig. 4. For negligible roughness magnitudes, the rolling friction is very close to the curve analytically calculated for smooth bodies [12,13]. The presence of surface irregularities at the contact interface increases the width of the apparent contact area, and reduces both the peak of the nominal contact pressure and the indentation amplitude. The net result is that the rolling friction decreases with increasing surface roughness (see below). The same is true for a ball-flat contact (contact region with radius r), where the dissipated energy is proportional to the volume $\sim r^3$ where the dissipation occurs, times the square of the strain amplitude. The strain $\varepsilon \approx u/r$ where $u = F/K \approx F/(Er)$ (where $K \approx Er$ is an effective spring constant). Thus the dissipated energy will scale with the radius of the contact region as $\sim r^3/r^4 \sim 1/r$, i.e. it decreases with increasing size r of the nominal contact region. A similar argument can be used to

show that also for the cylinder contact case the energy dissipation decreases with increasing surface roughness. However, this result is only valid as long as there is not an important contribution to the rolling friction from the asperity deformations.

The successful comparison presented in Fig. 3 confirms the validity of the viscoelastic macroscopic contact model.

3.2. Rubber hysteresis and mixed lubrication

In this section we discuss the combined effect of roughness and viscoelasticity on the frictional properties of a generic contact. We study the transition from the boundary (BL) to the hydrodynamic (HL) regime for the case of a smooth, rigid cylinder sliding on a semi-infinite viscoelastic solid (rubber) with a randomly rough surface. The rubber rheology is assumed to be described by a single relaxation time in order to reduce the set of contact parameters; results for real rubber will be presented later.

Fig. 5 shows the Stribeck curve, i.e. the friction coefficient as a function of the product $v_0\eta$ of the velocity v_0 and the viscosity η (red curve), as well as the different sources of energy dissipation. The sliding contribution (μ_{Sc} and μ_{Sf}) and the rolling contribution (i.e. the contribution from the hysteretic behavior of the contact) are shown separately. From dimensional arguments the mixed lubrication regime occurs for sliding velocities $v_{ML} \approx 10h_{rms}^2 E_r/(R\eta)$, whereas the largest values of the loss tangent (and therefore of rubber-induced rolling friction) occurs for $v_{GT} \approx a_0/\tau_r$, where η is the fluid viscosity, τ_r the rubber relaxation time and where a_0 is the half-width of the (infinitely long) rectangular (Hertz) contact region, calculated using the relaxed rubber modulus (in this case $a_0 \approx a_\infty$). In the simulation of Fig. 5, the rolling number $Q = v_{GT}/v_{ML} \approx (R^2\langle p\rangle\eta)/(10h_{rms}^2 E_r\tau_r) \approx 10^{-5}$, resulting in very different velocities where the maximum in the solid contact rolling friction μ_{Rc} occurs, and where the transition to the hydrodynamic regime occurs (see Fig. 5). It is interesting to observe that the highest values of the wet rolling friction μ_{Rf} (the friction resulting from the fluid pressure asymmetry), is of the same order of magnitude as the solid contact rolling friction μ_{Rc}, but shifted to much higher sliding velocities. Also note that μ_{Rf} is always comparable with the friction coming from the fluid shear stresses acting on the cylinder wall, μ_{Sf}, which includes both the contribution from the Couette and the Poiseuille flows. The condition $\mu_{Rf} \approx \mu_{Sf}$ is expected to hold only in soft contacts, where the shape of the average surface separation is far
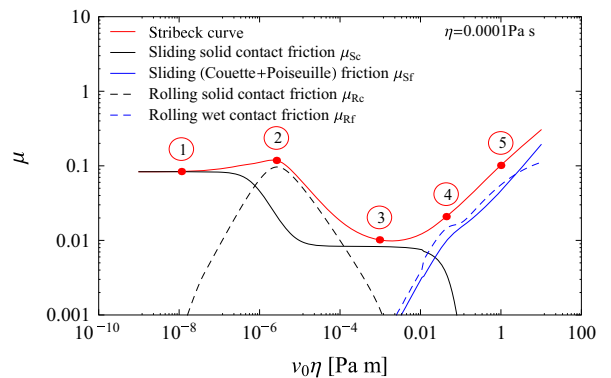

Fig. 5. (Colour online) Friction coefficient as a function of the product $v_0\eta$ (red curve), shown together with all the dissipation sources occurring in the lubricated (wet) rubber contact for $Q \approx 10^{-5}$. For a viscoelastic material characterized by one relaxation time $\tau_r = 0.1$ s and $E_\infty/E_0 = 10$, with $E_0 = 3.6$ MPa and $\nu = 0.5$. The cylinder radius $R = 1$ cm and the load $f_N = 1$ kN/m. For self-affine isotropic surface roughness with fractal dimension $D_f = 2.2$, low frequency cut-off $q_0 = 2 \cdot 10^5$ m^{-1}, high frequency cut-off $q_1 = 7.8 \times 10^9$ m^{-1}, and root-mean-square roughness $h_{rms} = 3 \, \mu$m. The solid contact shear stress $\sigma_c = 1$ MPa is assumed constant. Fluid viscosity $\eta = 10^{-4}$ Pa s.
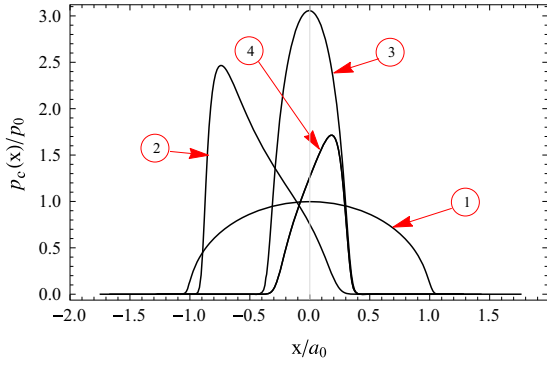
Fig. 6. Dimensionless average solid contact pressure p_c/p_0 as a function of the dimensionless contact position x/a_0. p_0 and a_0 refer, respectively, to the Hertz maximum pressure and semi-contact length occurring with the relaxed rubber (i.e. at E_0 elastic modulus). Curves shown at different sliding velocities, with numbered marks referring to Fig. 5. For the same parameters of Fig. 5.
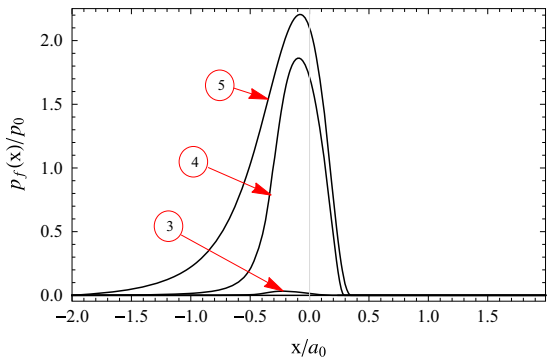

Fig. 7. Dimensionless average fluid pressure p_f/p_0 as a function of the dimensionless contact position x/a_0. p_0 and a_0 refer, respectively, to the Hertz maximum pressure and semi-contact length occurring with the relaxed rubber (i.e. at E_0 elastic modulus). Curves shown at different sliding velocities, with numbered marks referring to Fig. 5. For the same parameters of Fig. 5.

from being Grubin's like.[2] Due to the very different nature of the rubber and the fluid bulk rheologies, the rubber rolling friction as a function of velocity has a maximum related to the maximum of the loss tangent, whereas the fluid-pressure asymmetry, and its contribution to the friction, increases continuously with increasing sliding velocity.

The Stribeck curve in Fig. 5 shows an increase of the friction with decreasing velocity starting at $v_0\eta \approx 10^{-4}$ Pa m. This effect is not related to a transition from the fluid to asperity contact, but it is a consequence of the increase of the solid contact rolling friction (dashed black curve) and of the sliding contact friction (solid black curve) with decreasing sliding velocity. The increase of sliding contact friction with decreasing velocities can be explained observing that increasing the sliding velocity results in an increase of the effective elastic modulus $|E_r(\omega_H)|$ ($\omega_H \approx \pi v_0/a_H$), so that $\mu_{Sc} = \sigma_s A_c/F_N \sim \sigma_s/|E_r(\omega_H)|$ at low load where $A_c \sim F_N/|E_r(\omega_H)|$.

Figs. 6 and 7 show the (locally averaged) solid contact and fluid pressure fields, respectively, as a function of the contact position, at increasing sliding velocities (the numbered marks refer to Fig. 5). Note that, due to the small value of Q, the viscoelastic transition region occurs in the boundary lubricated (BL) regime and, as expected, it results (with increasing sliding velocity) in a

<hr>

[2] In 1949, Grubin presented the first accurate estimation of the film thickness in a steel–steel lubricated sliding contact (belonging to the hard-elastohydrodynamic regime). He postulated that during sliding, the solids would basically retain an Hertzian shape, with surfaces separated by a thin, uniform film of lubricant in the Hertzian area. Within this assumption, Grubin was able to analytically solve the lubrication problem.
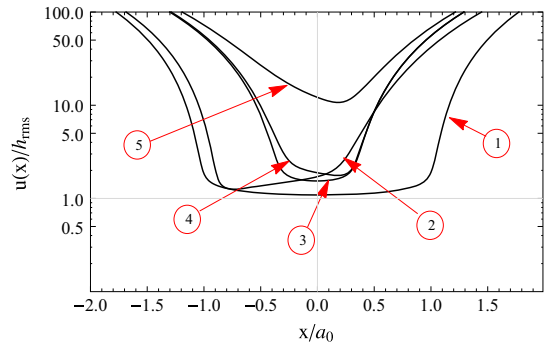

Fig. 8. Dimensionless average interfacial separation u/h_{rms} as a function of the dimensionless contact position x/a_0. Curves shown at different sliding velocities, with numbered marks referring to Fig. 5. For the same parameters of Fig. 5.
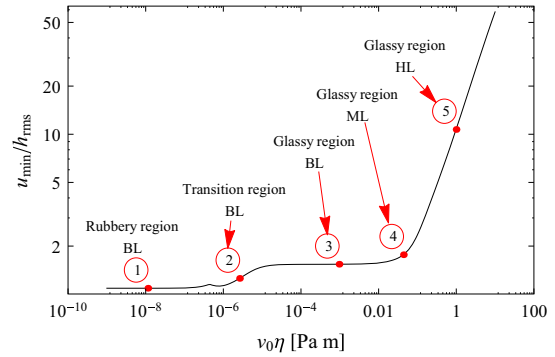

Fig. 9. Dimensionless minimum average interfacial separation u_{min}/h_{rms} as a function of the product sliding velocity and fluid viscosity. For the same parameters of Fig. 5.

reduction of the nominal contact length and the consequent increase of the average contact pressure, see Fig. 6. In particular, the short contact time (corresponding to high perturbing frequencies) at the inlet side of the contact results (for high enough sliding velocities) in a glassy (hard) rubber response, i.e. in higher contact pressures at the inlet side of the contact. However, upon a further increase of the sliding speed, the spike position is displaced toward the outlet of the contact, to finally disappear during the mixed lubrication regime. On the other hand, as the fluid pressure field is unaffected by the glassy transition (due to the small Q), the viscoelastic-hydrodynamic regime simply corresponds to the EHL regime for the stiff rubber elastic modulus E_∞.

Fig. 8 shows the average interfacial separation u as a function of contact position, at different sliding velocities. In contrast to elastic contacts, the minimum average interfacial separation is not strictly monotonically increasing with the sliding velocity. In particular, at the beginning of the viscoelastic transition region the minimum separation is located at the inlet first, and move toward the outlet at larger sliding velocities, as expected from the solid contact pressure curves. This is also shown in Fig. 9, where the minimum interfacial separation as a function of $v_0\eta$ is reported. Two plateau characterize the curve in the BL regime, with the lower value of separation corresponding to the contact in the rubbery region.

For the rolling number $Q \approx 1$ we expect a coupling between the viscoelastic and mixed lubrication transition regions. Fig. 10 shows the friction coefficient as a function of $v_0\eta$ (red line) and, separately, the rolling and sliding friction contributions for $Q \approx 0.3$. For elastic solids the minimum of the friction usually occurs in the mixed lubrication regime. For viscoelastic solids, however, when the rolling number ≈ 1 the maximum in the loss tangent roughly coincides with the mixed lubrication transition range of velocities, and this aspect strongly affects
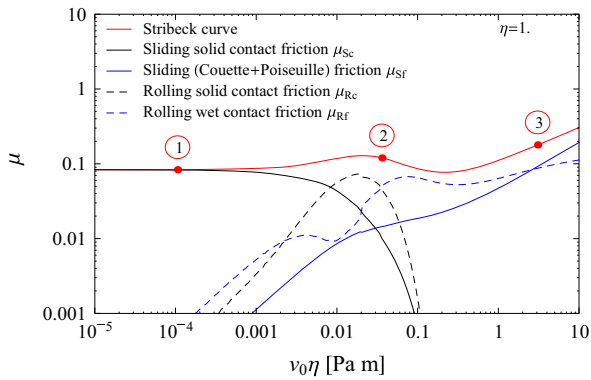
Fig. 10. (Colour online) Friction coefficient as a function of the product $v_0\eta$ (red curve), shown together with the all dissipation sources occurring in the rubber wet contact for $Q \approx 0.3$. For a viscoelastic material characterized by one relaxation time $\tau_r = 0.1$ s and $E_\infty/E_0 = 10$, with $E_0 = 3.6$ MPa and $\nu = 0.5$. The cylinder radius $R = 1$ cm and the load is $f_N = 1$ kN/m. For self-affine isotropic surface roughness with fractal dimension $D_f = 2.2$, low frequency cut-off $q_0 = 2 \times 10^5$ m^{-1}, high frequency cut-off $q_1 = 7.8 \times 10^9$ m^{-1}, and root-mean-square roughness $h_{rms} = 3$ μm. Solid shear stress set constant to 1 MPa. Fluid viscosity $\eta = 1$ Pa s.
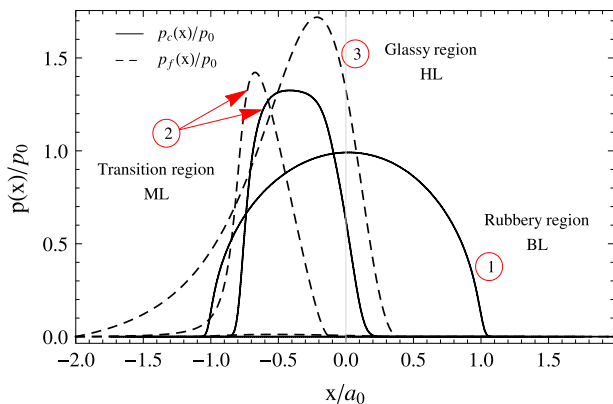
Fig. 11. Dimensionless average solid contact pressure p_c/p_0 and fluid pressure p_f/p_0 as a function of the dimensionless contact position x/a_0. p_0 and a_0 refer, respectively, to the Hertz maximum pressure and semi-contact length occurring with the relaxed rubber (i.e. at E_0 elastic modulus). Curves shown at different sliding velocities, with numbered marks referring to Fig. 10. For the same parameters of Fig. 10.

the Stribeck curve, both in the velocities where the frictional minimum occurs, as well as in the magnitude of the minimal friction. In particular, this could result in the occurrence of a second hydrodynamic regime (as indicated in Fig. 10), which could be erroneously attributed to local micro-EHL asperity contacts. In a recent experiment by one of us (MS), the existence of a similar secondary hydrodynamic regime was pointed out for a rough PDMS in contact with a sliding smooth ball [36]. However, in that case the origin of the double hydrodynamic regime was likely due to a cooperative micro-EHL effect occurring at the contact interface, i.e. the frictional collection of local micro-elastohydrodynamic lubrication conditions at the asperities scale [note: the friction enhancement could not have been ascribed to a rubber hysteretic effect, since the sliding contact was probed in its relaxed configuration (steady rubber in contact with a rotating ball)]. Observe also (see Fig. 10) that both the rolling friction sources (μ_{Rc} and μ_{Rf}) are of the same order of magnitude during the viscoelastic and mixed lubrication transitions and, moreover, the wet rolling friction is roughly one order larger that the wet sliding friction. The latter phenomenon is very interesting, but is not a surprise since the transfer of normal load from the asperity contacts

determines an increase of the locally averaged fluid pressure as compared to the solid contact pressure. As a consequence, the rubber is hysteretically stimulated by the fluid–asperity interactions as well, resulting in the remarkable increase of the wet rolling dissipation with respect to the wet sliding friction.

Fig. 11 shows the (locally averaged) solid contact (solid line) and fluid pressure (dashed) fields as a function of the contact position, at different sliding velocities. The concurrent occurrence of the ML and glassy transition determines, interestingly, the appearance of the inlet spike on both pressure fields, as highlighted with the number-2 mark in the figure.

The results presented above shows that the classical way of presenting the Stribeck curve, with the friction coefficient as a function of ηv_0, is less useful for viscoelastic solids as it does not take into account the viscoelastic behavior of the contact. That is, the construction of a smooth master-curve for μ as a function of ηv_0 by combining measurements using different fluid viscosities will in general be impossible, in particular when non-negligible hysteretic contributions from bulk viscoelasticity are expected to occur in a short range of relaxation times.

To illustrate this, Fig. 12 shows the friction coefficient μ as a function of $v_0\eta$, calculated with the same surface roughness and rubber rheology as in Figs. 5 and 10, but for different viscosity values (equally spaced in a log$_{10}$ scale). In the figure, the mixed lubrication transition occurs for all viscosities in a range of $v_0\eta$ which is close to the marked red line (determined by the sliding reduced velocity value $v_0\eta$ at which the normal load is equally shared by asperity- and fluid–asperity interactions). Interestingly, for a viscoelastic solid the mixed lubrication transition cannot be determined by looking to the macroscopic characteristics of the contact such as friction. Indeed, apparent secondary hydrodynamic as well as apparent mixed lubrication regimes are characterizing the generic wet sliding rubber contact. As an example, for the lower fluid viscosity the apparent mixed lubrication transition occurs at $v_0\eta \approx 10^{-6}$ Pa m, i.e. four velocity decades before the real mixed lubrication transition. Moreover, observe that the Stribeck curves do not overlap. This is very interesting and suggests that the viscoelastic effect can be used, as recently shown for the case of micro-EHL, to tune the friction of wet sliding rubber contacts. Indeed, observe that for the before-last value of viscosity ($Q \approx 1$), the friction is kept to large values in the entire range of sliding velocities. On the contrary, the smallest values of rolling parameters Q can help to strongly decrease the friction in a remarkably wide range of sliding velocities. This suggests that an accurate understanding of the soft contact mechanics could help to produce tailored friction pairs in applications such as, e.g., tire-road
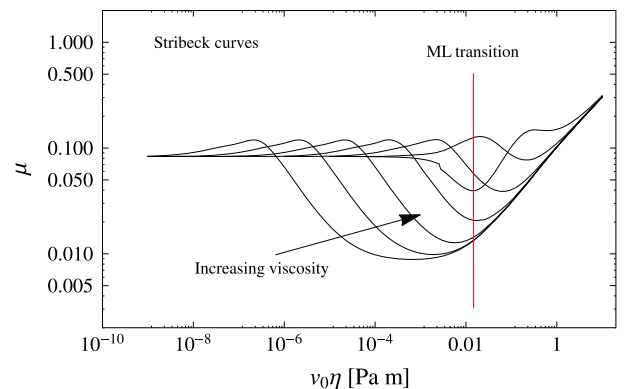

Fig. 12. (Colour online) Stribeck curves as a function of the product $v_0\eta$. The vertical red line mark indicates the mixed lubrication transition. For different values of fluid viscosity.
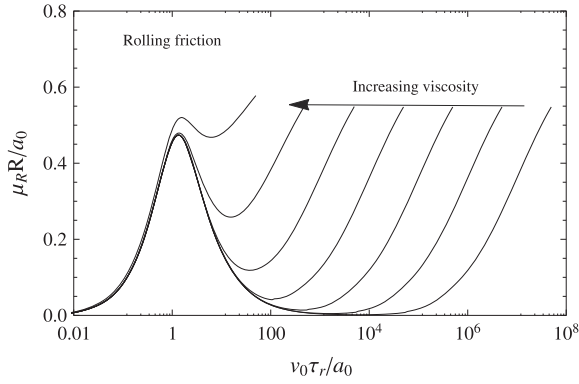
Fig. 13. Total rolling friction ($\mu_{Rs} + \mu_{Rf}$) as a function of the dimensionless sliding velocity $v_0 \tau_r / a_0$. For different values of fluid viscosity.
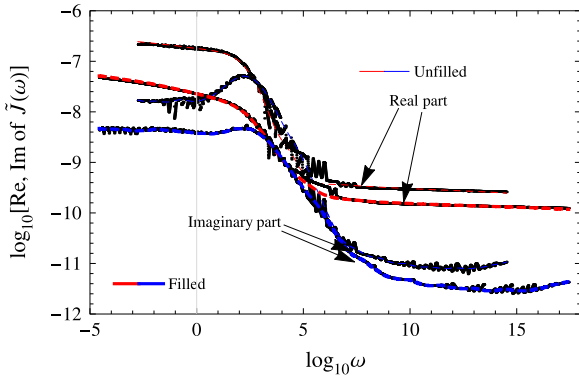

Fig. 14. (Colour online) Real and imaginary part of the complex creeping function $\tilde{J}(\omega) = 1/E(\omega)$ as measured (dots) and fitted by Prony series (dashed blue and red curves). For unfilled (thick line) and filled rubber. In $\log_{10} - \log_{10}$, with $|\tilde{J}|$ in Pa^{-1} and ω in s^{-1}.

Fig. 15. (Colour online) Friction coefficient as a function of the product $v_0 \eta$ (red curve), shown together with all the dissipation sources occurring in the rubber wet contact for $Q = 3 \times 10^{-4}$. For the unfilled rubber. The cylinder radius $R = 1$ mm and the load is $f_N = 117$ N/m. For self-affine isotropic surface roughness with fractal dimension $D_f = 2.2$, low frequency cut-off $q_0 = 2 \; 10^5 \; m^{-1}$, high frequency cut-off $q_1 = 7.8 \times 10^9 \; m^{-1}$, and root-mean-square roughness $h_{rms} = 0.5 \; \mu m$. Solid shear stress set constant to 1 MPa. Fluid viscosity $\eta = 0.001$ Pa s.
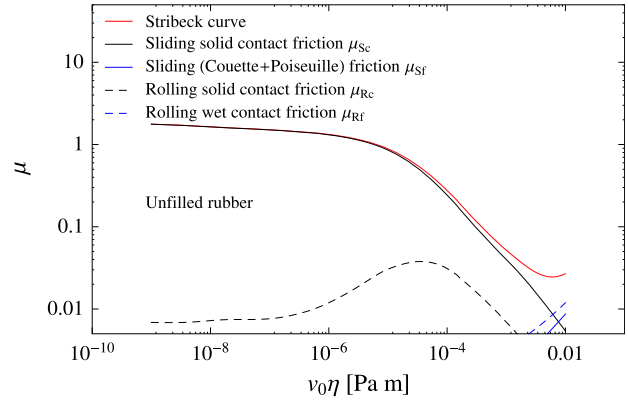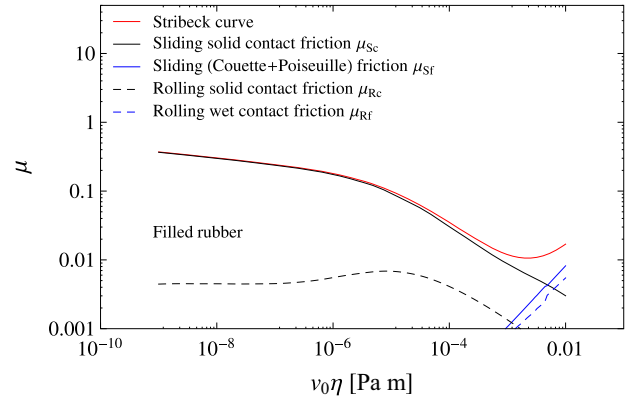

Fig. 16. (Colour online) Friction coefficient as a function of the product $v_0 \eta$ (red curve), shown together with all the dissipation sources occurring in the rubber wet contact for $Q = 3 \times 10^{-5}$. For the filled rubber. The cylinder radius $R = 1$ mm and the load is $f_N = 117$ N/m. For self-affine isotropic surface roughness with fractal dimension $D_f = 2.2$, low frequency cut-off $q_0 = 2 \times 10^5 \; m^{-1}$, high frequency cut-off $q_1 = 7.8 \times 10^9 \; m^{-1}$, and root-mean-square roughness $h_{rms} = 0.5 \; \mu m$. Solid shear stress set constant to 1 MPa. Fluid viscosity $\eta = 0.001$ Pa s.

sliding contact (where high friction is required) and dynamical rubber sealing (where low friction is required).

Fig. 13 shows the rolling friction dissipation ($\mu_{Rc} + \mu_{Rf}$) as a function of the Deborah number $v_0 \tau_r / a_0$ for different values of fluid viscosity. Note that the fluid strongly modifies the classical rolling friction curve. On the lower velocity side all curves overlap as expected, since the contribution to the friction from the fluid shearing is negligible. However, increasing the sliding velocity or the fluid viscosity shows up the (non-bounded) rolling dissipation behavior of the fluid. This also suggests that estimating (even approximately) the contribution to the rolling friction for wet contacts using results (from experiment or theory) for dry contact may not allow to capture the correct physics or magnitude of the rolling friction contribution [37,38].

4. Numerical results: real rubber

Viscoelastic solids such as rubber have usually a very wide distribution of relaxation times. Fig. 14 shows the complex creep [$\tilde{J}(\omega) = 1/E(\omega)$] of an unfilled and filled rubber compound. In particular, the real and imaginary part of $1/E(\omega)$ as measured (dots) and fitted by Prony series (dashed blue and red curves) are reported.

We have calculated the sliding friction (cylinder on flat) for the compounds in Fig. 14 in water environment (viscosity $\eta = 0.001$ Pa s), for a self-affine isotropic roughness with fractal dimension $D_f = 2.2$, low frequency cut-off $q_0 = 2 \times 10^5 \; m^{-1}$, high frequency cut-off $q_1 = 7.8 \times 10^9 \; m^{-1}$, and the root-mean-square roughness $h_{rms} = 0.5$ and $5 \; \mu m$. The interfacial shear stress

$\sigma_s = 1$ MPa. In Figs. 15 and 16 we show, respectively, the Stribeck curve, i.e., the friction coefficient as a function of $v_0 \eta$, for the unfilled and filled rubber at $h_{rms} = 0.5 \; \mu m$ ($Q_{fil} = 3 \times 10^{-5}$, $Q_{unfil} = 3 \times 10^{-4}$). Note that due to the different stiffness characteristics, the unfilled rubber has a larger friction than the filled one, in almost all the range of sliding velocities. The same fact is observed in Fig. 17, where we show Stribeck curves at different values of rubber root mean square roughness, and is due to the larger real contact area (which increases the sliding solid contact friction μ_{Sc}) and to the larger loss tangent in the unfilled compound (which increases the rolling friction μ_{Rc}). The minimum interfacial separation as a function of sliding velocities is shown in Fig. 18 for the unfilled and filled rubbers, respectively. Note that for the unfilled case the minimum separation is not increasing monotonically with $v_0 \eta$: an increasing indentation in the rubber occurs for $v_0 \eta \approx 10^{-5}$ Pa m, which corresponds to a velocity in the viscoelastic transition region. For the filled rubber the minimum separation, instead, monotonically grows with increasing sliding speed.

Note that for real rubbers the Stribeck curves (Fig. 17), differently from the separation curves (Fig. 18), seem not to quantitatively
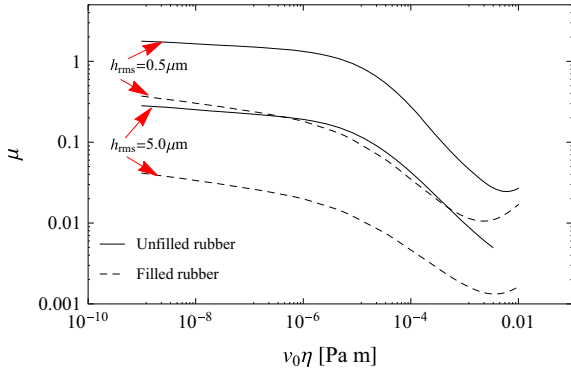
Fig. 17. Stribeck curves as a function of the product $v_0\eta$ for the two different rubber compounds. For $h_{rms} = 0.5$ and 5 µm.
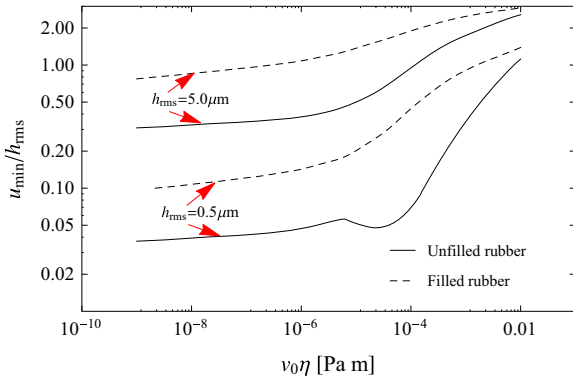

Fig. 18. Dimensionless minimum average interfacial separation u_{min}/h_{rms} as a function of the product $v_0\eta$ for the two different rubber compounds. For $h_{rms} = 0.5$ and 5 µm.

show the dissipation mechanisms highlighted for simple rubber rheologies (discussed in Section 3.2). However, this is mainly ascribed to the particular operating conditions adopted in the calculations of Figs. 15–17, and less to the widening or suppression of the dissipations modes of the particular rubber compound. As an example, temperature is well known to enormously affect the viscoelastic response of a generic rubber, e.g. an increase of ~ 5 degrees may shift the complex elastic modulus curves reported in Fig. 14 by one decade along the frequency axis (toward higher frequencies). Hence, with respect to Fig. 15, a temperature increase of about ten degrees of the rubber (at constant fluid viscosity) could result in a rolling number ≈ 1 and, therefore, of a friction curve similar to that observed in Fig. 10.

Finally, we observe that the model developed above can help predicting the optimal viscoelastic spectrum to obtain a particular lubrication condition, e.g., to couple (uncouple) the different mechanisms of dissipation occurring in a wet contact in order to maximize (minimize) the friction coefficient.

5. Conclusions

We have described the different sources of friction prevailing in the steady sliding of a hard cylinder on a wet viscoelastic solid with surface roughness, as often encountered in rubber and bio-tribology applications. We have discussed the role of the rubber viscoelasticity and of the (fluid) viscosity in determining the Stribeck curve $\mu(v)$, for both simple (model) and real (measured) rubber rheologies. In particular, rubber viscoelasticity may result in apparent (or false) mixed and hydrodynamic regimes, which are instead a consequence of the contact stiffening. Moreover, depending on the rubber
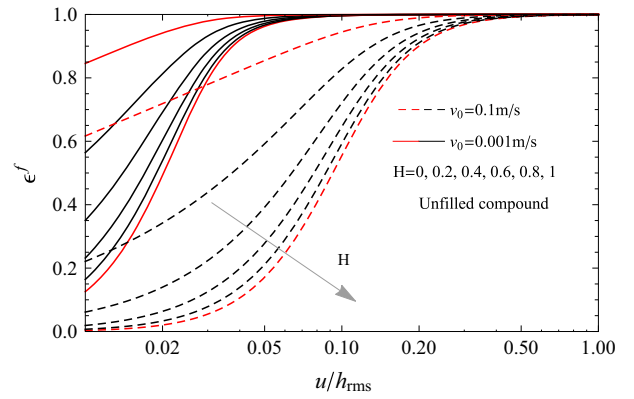

Fig. 19. (Colour online) The intensity of the fluid–asperity interactions, expressed in term of ε_f, as function of the normalized average separation. Red curves corresponds to limiting values of H. For the unfilled rubber and for self-affine isotropic surface roughness with low frequency cut-off $q_0 = 2 \times 10^5$ m^{-1}, high frequency cut-off $q_1 = 7.8 \times 10^9$ m^{-1}, and root-mean-square roughness $h_{rms} = 3$ µm. Fluid viscosity $\eta = 0.01$ Pa s.

Fig. 20. (Colour online) The intensity of the fluid–asperity interactions, expressed in term of ε_f, as function of the normalized average separation. Red curves corresponds to limiting values of H. For the filled rubber and for self-affine isotropic surface roughness with low frequency cut-off $q_0 = 2 \times 10^5$ m^{-1}, high frequency cut-off $q_1 = 7.8 \times 10^9$ m^{-1}, and root-mean-square roughness $h_{rms} = 3$ µm. Fluid viscosity $\eta = 0.01$ Pas.
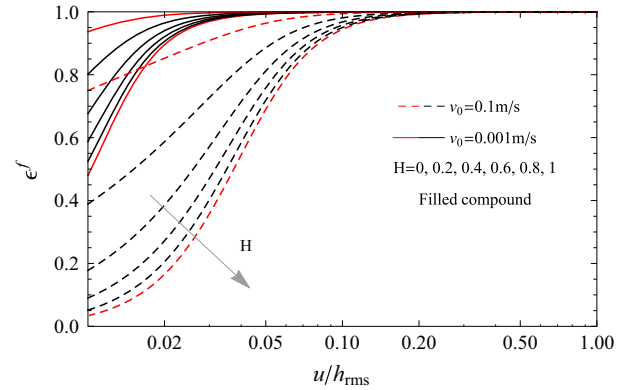
viscoelastic characteristics, the standard procedure to obtain a friction mastercurve (Stribeck curve) by using different fluid viscosities, and plotting the friction coefficient as a function of ηv, may not work for viscoelastic solids. Finally, we have shown that the rubber viscoelastic modulus and surface roughness may be chosen or designed to obtain a $\mu(v)$ curve suitable for a particular application.

Acknowledgments

Appendix A

For the line contact case, Eq. (20) can be discretized as following. In particular, the average interfacial separation is

$$u(x) = u(x_0) + f_{shape}(x) + w(x) - w(x_0),$$

where the out-of-plane displacement field reads

$$w(x) = -\frac{2}{\pi}\frac{1-\nu^2}{E_\infty}\int dx' p_0(x')\log|x-x'|$$
$$-\frac{2}{\pi}\frac{1-\nu^2}{E_\infty}\int dx' p_0(x')\int_0^\infty dt\ \Gamma(t)\log\ |x+tv_0-x'|.$$

By integrating the elastic term of the surface displacement on a grid space of length δ, the well know discrete elastic kernel is recovered:

$$\frac{D_E^{1D}(x)}{\frac{2}{\pi}\frac{1-\nu^2}{E_\infty}p_0} = \delta\left(1-\frac{1}{2}\log\left|x^2-\frac{\delta^2}{4}\right|\right) - x\log\left|\frac{x+\delta/2}{x-\delta/2}\right|,$$

whereas the viscoelastic term can be determined as follows:

$$\frac{D_{VE}^{1D}(x)}{\frac{2}{\pi}\frac{1-\nu^2}{E_\infty}p_0} = \int_0^\infty dt\ \Gamma(t)D_E^{1D}(x+tv_0) = E_\infty\int_0^\infty d\tau L(\tau)d_{ve}^{1D}(x,v_0\tau),$$

where $L(\tau)$ is the creep spectrum, with $d_{ve}^{1D}(x,v_0\tau) = \int_0^\infty dt\ e^{-t}D_E^{1D}(x+tv_0\tau)$, which can be integrated to give

$$d_{ve}^{1D}(x,v_0\tau) = \delta\left(1-\frac{v_0\tau+x}{\delta}\log\left|\frac{x+\delta/2}{x-\delta/2}\right| - \frac{\log\left|x^2-\frac{\delta^2}{4}\right|}{2}\right)$$
$$+ v_0\tau\left[e^{(x+\delta/2)/(v_0\tau)}\exp_{Ei}\left(-\frac{x+\delta/2}{v_0\tau}\right)\right]$$
$$+ v_0\tau\left[-e^{(x-\delta/2)/(v_0\tau)}\exp_{Ei}\left(\frac{x-\delta/2}{v_0\tau}\right)\right].$$

Therefore, for the cylinder contact case the discrete viscoelastic kernel for the half space has an *analytical* expression as for the elastic case. By considering the creep spectrum as decomposed in an array of N_τ relaxation times:

$$L(\tau) = \frac{1}{E_\infty}\sum_{i=1}^{N_\tau} A_i\delta(\tau-\tau_{ri}), \tag{22}$$

we have

$$\frac{D_{VE}^{1D}(x)}{\frac{2}{\pi}\frac{1-\nu^2}{E_\infty}p_0} = \sum_{i=1}^{N_\tau} A_i d_{ve}^{1D}(x,v_0\tau_{ri}).$$

The discrete viscoelastic kernel (of grid length δ) to be used in the average macroscopic deformation of the rubber surface can then be easily determined:

$$D^{1D}(x) = D_E^{1D}(x) + \frac{2}{\pi}\frac{1-\nu^2}{E_\infty}p_0\sum_{i=1}^{N_\tau} A_i d_{ve}^{1D}(x,v_0\tau_{ri}).$$

Appendix B

Here it is considered the case where a rubber block in a traction experiment behaves with a complex elastic modulus given by a spring E_∞ in series with a paired E_2 spring and $\tau_r E_2$ dashpot:

$$\frac{E(\omega)}{E_\infty} = \frac{1-i\omega\tau_r}{1+E_\infty/E_2-i\omega\tau_r}.$$

The previous complex elastic modulus can be also obtained from Eq. (14) for $L(\tau) = E_\infty^{-1}A\delta(t-\tau_r)$ (single relaxation time), when $E_\infty/E_2 = A$. In such a case the viscoelastic component of the discrete deformation kernel is simply given by

$$\frac{D_{VE}^{1D}(x)}{\frac{2}{\pi}\frac{1-\nu^2}{E_\infty}p_0} = \frac{E_\infty}{E_2}\ d_{ve}^{1D}(x,v_0\tau_r).$$

The previous result can also be obtained by making use of the creep function [39] $J(t)$:

$$J(t) = H(t)\left[J(t=0) + \int_0^\infty d\tau L(\tau)(1-e^{-t/\tau})\right],$$

where $H(t)$ is the Heaviside step and $J(t=0) = E_\infty^{-1}$. $J(t)$ is simply related to $\Gamma(t)$ with $\Gamma(t) = E_\infty[\partial J/\partial t]_{t>0}$, whereas the complex creep function $\tilde{J}(\omega)$ can be linked to the Fourier transform of the real creep function with

$$\tilde{J}(\omega) = i\omega J(\omega) = E(\omega)^{-1},$$

from which the complex elastic modulus can be obtained.

Appendix C

Here we characterize the fluid-induced asperity flattening [24] occurring at the interface of our viscoelastic contact. In the reference associated to a representative moving control volume, the frequency representation of the displacement field reads

$$u_z(\mathbf{q},\omega) = \frac{-2}{q\ E_r(\omega-\mathbf{q}\cdot\mathbf{v}_R)}p(\mathbf{q},\omega),$$

where $\mathbf{q}$ is the wave-vector, ω the pulsating frequency, and $\mathbf{v}_R$ is the half space translational velocity relative to the control volume. Now we focus on the surface height fluctuations included in the representative elementary volume of contact (REV). Assuming that the two surfaces are sliding one against the other at different constant velocities $\mathbf{v}_1$ and $\mathbf{v}_2$ (relative to the REV, with 1-subscript indicating the lower surface, and 2- the upper surface), the roughness occurring at the interface can be described with $h_r(\mathbf{x},t) = h_{r1}(\mathbf{x}-\mathbf{v}_1 t) + h_{r2}(\mathbf{x}-\mathbf{v}_2 t)$, whereas in the frequency domain: $h_r(\mathbf{q},\omega) = h_{r1}(\mathbf{q})\delta(\omega-\mathbf{q}\cdot\mathbf{v}_1) + h_{r2}(\mathbf{q})\delta(\omega-\mathbf{q}\cdot\mathbf{v}_2)$. $h_r(\mathbf{x},t)/u << 1$ usually. At first order in the fluid pressure field, $p_1(\mathbf{q},\omega)$ (first order fluid pressure) is correlated to $u_z(\mathbf{q},\omega)$ (first order out-of-plane displacement) by

$$u_z(\mathbf{q},\omega) = K^c(q,\omega)p_1(\mathbf{q},\omega), \tag{23}$$

where $K^c(q,\omega) = -2/[E_r(\omega-\mathbf{q}\cdot\mathbf{v}_R)q]$, as calculated before. Thus the first order separation fluctuation reads

$$h(\mathbf{q},\omega) = h_{r1}(\mathbf{q})\delta(\omega-\mathbf{q}\cdot\mathbf{v}_1) + h_{r2}(\mathbf{q})\delta(\omega-\mathbf{q}\cdot\mathbf{v}_2)$$
$$+ K^c(q,\omega)p_1(\mathbf{q},\omega). \tag{24}$$

The first order fluid pressure $p_1(\mathbf{q},\omega)$, caused by the fluctuating surface profiles, has been shown to be obtained by perturbing the thin film fluid flow equation, and by collecting the first orders [24]:

$$p_1(\mathbf{q},\omega) = h(\mathbf{q},\omega)K^f(\mathbf{q},\omega), \tag{25}$$

where the kernel $K^f(\mathbf{q},\omega)$ is

$$K^f(\mathbf{q},\omega) = i\left[\frac{3\mathbf{q}\cdot\nabla p_f}{uq^2} - \frac{12\mu(\omega+\mathbf{q}\cdot\mathbf{v}_m)}{u^3 q^2}\right].$$

Substituting Eq. (24) in Eq. (25) we determine the relation, in the Fourier space, between the separation fluctuation (deformed by the same fluid action) and the first order fluid pressure $p_1(\mathbf{q},\omega)$, resulting in

$$p_1(\mathbf{q},\omega) = G(\mathbf{q},\omega)$$
$$\times[h_{r1}(\mathbf{q})\delta(\omega-\mathbf{q}\cdot\mathbf{v}_1) + h_{r2}(\mathbf{q})\delta(\omega-\mathbf{q}\cdot\mathbf{v}_2)], \tag{26}$$

where the kernel $G(\mathbf{q},\omega)$ describes the interaction between the fluid particles and the asperities (local fluid–structure interactions, lFSI) of the rough surfaces:

$$G(\mathbf{q},\omega) = \frac{K^f(\mathbf{q},\omega)}{1-K^f(\mathbf{q},\omega)K^c(\mathbf{q},\omega)}. \tag{27}$$

It is interesting to note that Eq. (27) converges to $[-K^c(q,\omega)]^{-1}$ for average separations close to zero, so that the transition from lubricated to boundary lubricated conditions occurs smoothly. The average square separation fluctuation can be calculated by substituting Eq. (26) in Eq. (24), resulting into (after some algebra) $\langle h^2 \rangle = \langle h_1'^2 \rangle + \langle h_2'^2 \rangle$, with

$$\langle h_i'^2 \rangle = \varepsilon^s(u) \times \int d^2q |1 + K^c(q, \mathbf{q} \cdot \mathbf{v}_i)G(\mathbf{q}, \mathbf{q} \cdot \mathbf{v}_i)|^2 C_i(\mathbf{q}), \tag{28}$$

where $\varepsilon^s(u)$ is the apparent roughness smoothening parameter originating from the occurrence of solid contact areas, see Ref. [24]. However, here we only focus on the viscous-induced asperity flattening, described by the function $\lambda_i(\mathbf{q}, u, \nabla p_f) \geq 1$ (which modulates the power spectral density, see Eq. (28)):

$$\frac{1}{\lambda_i(\mathbf{q}, u, \nabla p_f)} = [1 + K^c(q, \mathbf{q} \cdot \mathbf{v}_i)G(\mathbf{q}, \mathbf{q} \cdot \mathbf{v}_i)|^2.$$

Since

$$1 + K^c(q, \mathbf{q} \cdot \mathbf{v}_i)G(\mathbf{q}, \mathbf{q} \cdot \mathbf{v}_i) = \frac{1}{1 - iK^c K^f},$$

we have

$$\lambda_i(\mathbf{q}, u, \nabla p_f) = (1 + 2k_{im}^c(\mathbf{q} \cdot \mathbf{v}_i)k_{im}^f(q, \mathbf{q} \cdot \mathbf{v}_i)K(q))^2$$
$$+ (k_{re}^c(\mathbf{q} \cdot \mathbf{v}_i)k_{im}^f(q, \mathbf{q} \cdot \mathbf{v}_i)K(q))^2, \tag{29}$$

where $K^f(q, \mathbf{q} \cdot \mathbf{v}_i) = ik_{im}^f(q, \mathbf{q} \cdot \mathbf{v}_i)$. Moreover, by using the Prony series for the viscoelastic rheological description, $L(\tau) = E_\infty^{-1} \sum_i A_i \delta(\tau - \tau_{ri})$, and by considering $K(q) = -2/[E_{r\infty}q]$:

$$K^c(q, \mathbf{q} \cdot \mathbf{v}_i) = K(q)[k_{re}^c(\mathbf{q} \cdot \mathbf{v}_i) + ik_{im}^c(\mathbf{q} \cdot \mathbf{v}_i)],$$

with

$$k_{re}^c(\mathbf{q} \cdot \mathbf{v}_i) = 1 + \sum_i \frac{A_i}{1 + [\tau_{ri}\mathbf{q} \cdot (\mathbf{v}_i - \mathbf{v}_r)]^2}$$

$$k_{im}^c(\mathbf{q} \cdot \mathbf{v}_i) = \mathbf{q} \cdot (\mathbf{v}_i - \mathbf{v}_r) \sum_i \frac{A_i \tau_{ri}}{1 + [\tau_{ri}\mathbf{q} \cdot (\mathbf{v}_i - \mathbf{v}_r)]^2}.$$

Observe that $k_{im}^f(q, \mathbf{q} \cdot \mathbf{v}_i)K(q)$ can be rephrased in Eq. (29) with

$$k_{im}^f(q, \mathbf{q} \cdot \mathbf{v}_i)K(q)$$
$$= -\frac{6}{\zeta^2}\left[\frac{1}{u/h_{rms}q_0^2 h_{rms}E_{r\infty}} \frac{\nabla p_f}{q} \cdot \frac{\mathbf{q}}{q}\right] + \frac{6}{\zeta^2}\left[\frac{1}{u^3/h_{rms}^3} \frac{4\mu[2\mathbf{v}_m \pm \Delta\mathbf{v}]}{q_0^2 h_{rms}^3 E_{r\infty}} \cdot \frac{\mathbf{q}}{q}\right],$$

with $\Delta\mathbf{v} = (\mathbf{v}_2 - \mathbf{v}_1)/2$, $\mathbf{v}_m = (\mathbf{v}_2 + \mathbf{v}_1)/2$ and $\zeta = q/q_0$. We can finally define a lFSI parameter $0 \leq \varepsilon_i^f \leq 1$, with $i=1$ (lower surface) or 2 (upper surface):

$$\varepsilon_i^f(u, \nabla p_f) = \int d^2q \frac{C_i(\mathbf{q})}{\lambda_i(\mathbf{q}, u, \nabla p_f)} / \int d^2q C_i(\mathbf{q}), \tag{30}$$

which characterizes the intensity of the fluid–asperity interaction occurring on the i-indexed surface: the more $\varepsilon_i^f \rightarrow 0$ the more intense is the viscous flattening [24]. The effect of fluid–asperity interactions on the local separation is completely captured by the parameter $\lambda_i(\mathbf{q}, u, \nabla p_0)$ which, because of the viscoelastic nature of the solids, presents a more complex formulation with respect to the elastic case [24]. In particular, the amplitudes of the spectral components of the fluid film thickness are given by the weighted sum of the spectral amplitudes of the original undeformed rough surfaces (where the weights are given by λ_i^{-1}) multiplied by the smoothing parameter $\varepsilon^s(u)$, resulting in an average separation fluctuation $\langle h^2 \rangle = \varepsilon^s (\varepsilon_1^f h_{rms,1}^2 + \varepsilon_2^f h_{rms,2}^2)$ [24]. The presence of local squeeze motions, combined to the viscous action coming from the flow driving term $\mathbf{v}_m$, determines different λ_i parameters for the two surfaces.

In our contact case, only the viscoelastic half space is covered by roughness ($C_2(\mathbf{q}) = 0$), and we have $v_2 = 0$ and $v_R = v_1$. We then expect $k_{re}^c(\mathbf{q} \cdot \mathbf{v}_i) = 1 + \sum_i A_i$ and $k_{re}^c(\mathbf{q} \cdot \mathbf{v}_i) = 0$, i.e. the fluid-induced

asperities flattening occurs under a relaxed rubber deformation. However, the time-frequency at which asperities are deformed by the fluid action, even in the present case, is not exactly zero, but has a physical zero given by the lowest pulsating deformation at frequency $\omega_H \approx \pi v/a_H$. Therefore we use

$$k_{re}^c = 1 + \sum_i \frac{A_i}{1 + [\tau_{ri}(\pi v/a_H)]^2}; \quad k_{im}^c = (\pi v/a_H) \sum_i \frac{A_i \tau_{ri}}{1 + [\tau_{ri}(\pi v/a_H)]^2},$$

where $a_H^2 = 4f_N R/(\pi|E_r(\omega_H)|)$. Finally, by neglecting the average fluid pressure gradient source of viscous flattening ($\nabla p_f \approx 0$):

$$k_{im}^f(q, \mathbf{q} \cdot \mathbf{v}_i)K(q) = \frac{1}{u^3/h_{rms}^3 \zeta^2} 6F_s\left(\mathbf{e}_1 \cdot \frac{\mathbf{q}}{q}\right),$$

where $\mathbf{e}_1$ is the unit vector along the sliding direction, and where a viscous flattening source F_s can be defined as

$$F_s = \frac{6\mu v_0}{q_0^2 h_{rms}^3 E_{r\infty}}.$$

Hence, by using $\mathbf{q} = q\{\cos\theta, \sin\theta\}$, we have $\lambda_1(\mathbf{q}, u, \nabla p_f) = \lambda(\zeta = q/q_0, \theta, u)$ to be used in Eq. (30):

$$\lambda(\zeta = q/q_0, \theta, u) = \left(1 + 2k_{im}^c \frac{1}{u^3/h_{rms}^3 \zeta^2} 6F_s \cos\theta\right)^2$$
$$+ \left(k_{re}^c \frac{1}{u^3/h_{rms}^3 \zeta^2} 6F_s \cos\theta\right)^2. \tag{31}$$

As a further result, not shown for simplicity, in the present contact case, the mean square deformed roughness $\langle h_1^2 \rangle$ covering the viscoelastic half space can be shown to be equal to the mean square separation $\langle h^2 \rangle = \langle h_1'^2 \rangle = \langle h_1^2 \rangle$.

In Figs. 19 and 20, respectively for the filled and unfilled rubber, ε_f is shown as a function of the average interfacial separation for different values of roughness fractal dimensions D_f. The adopted roughness is isotropic and self-affine, with $q_0 = 2 \times 10^5$ m^{-1}, $q_1 = 7.8 \times 10^9$ m^{-1} and $h_{rms} = 3$ μm, the fluid viscosity $\eta = 0.01$. Observe first that, in both cases, even to large sliding velocities (curves at 0.1 m/s), a nonnegligible flattening occurs only for values of average interfacial separations u/h_{rms} of order 0.1, a value common for high pressure rubber contacts (as tire contacts). Moreover, note that increasing the sliding velocity by two orders of magnitude does not strongly affect the magnitude of the viscous flattening. Indeed, increasing the sliding velocity increases both the fluid shearing action and the elastic modulus of the local asperities (as a consequence of the rubber stiffening). Therefore, the (local) deformations induced by the (local) pressure gradients are markedly attenuated in real rubbers. Observe finally that by reducing the Hurst exponent H, which is related to the fractal dimension as $D_f = 3 - H$, the viscous flattening is less effective. This must not surprise since larger fractal dimensions, for a fixed value of mean-square-roughness, correspond to a larger content of small scale surface fluctuations, which are well known (see e.g. Eq. (31)) to be less affected by viscous flattening.

Appendix D

Eqs. (3), (7), (8), (20) and (21) have been solved with two different approaches depending on the lubrication regime. In particular, we adopted the BLP and MHLS algorithms, successfully applied in Ref. [23] for the resolution of the mixed-elastohydrodynamic soft lubrication problem, with two major modifications. In particular, due to the loss of diagonal dominance in the discrete formulation of

Eq. (20) as Fredholm equation, we have adopted the LU decomposition for determining the Newton step at the generic iteration. Moreover, the (implicit) resolution of Eq. (21) as a function of u_0 is not successful by choosing $u_0 = u(x = 0)$. Indeed, due to the non-monotonic increase of the minimum and central average separation as a function of the reduced sliding speed $v_0\eta$, u_0 has been chosen to be $u_0 = u(\overline{x}_0)$, with $\overline{x}_0 = f_N^{-1} \int dx\, x p_0(x)$. Thus, the position $\overline{x}_0$ of the reference separation u_0 changes by changing the sliding speed, allowing to stabilize the numerical scheme.

References

[1] Persson BNJ. Rubber friction and tire dynamics. J Phys Condens Matter 2011;23(1):01500323.
[2] Salant RF. Theory of lubrication of elastomeric rotary shaft seals. Proc Inst Mech Eng Part J 1999;213(3):189–201.
[3] Scaraggi M, Carbone G. A two-scale approach for lubricated soft-contact modeling: an application to lip-seal geometry. Adv Tribol 2012:412190.
[4] Bódai G, Goda TJ. Friction force measurement at windscreen wiper/glass contact. Tribol Lett 2012;45(3):515–23.
[5] Adams MJ, Briscoe BJ, Johnson SA. Friction and lubrication of human skin. Tribol Lett 2007;26(3):239–53.
[6] Dunn AC, Uruena JM, Huo Y, Perry SS, Angelini TE, Sawyer WG. Lubricity of surface hydrogel layers. Tribol Lett 2013;49:371–8.
[7] Kovalev AE, Varenberg B, Gorb SN. Wet versus dry adhesion of biomimetic mushroom-shaped microstructures. Soft Matter 2012;8(29):7560–6.
[8] Ateshian GA. The role of interstitial fluid pressurization in articular cartilage lubrication. J Biomech 2009;42:1163–76.
[9] Accardi MA, McCullen SD, Callanan A, Chung S, Cann PM, Stevens MM, Dini D. Effects of fiber orientation on the frictional properties and damage of regenerative articular cartilage surfaces. Tissue Eng Part A 2013;19(19–20):2300–10.
[10] Lorenz B, Krick B, Rodriguez N, Sawyer WG, Mangiagalli P, Persson BNJ. Static or breakloose friction for lubricated contacts: role of surface roughness and dewetting. J Phys: Condens Matter 2013;25(44):445013.
[11] Persson BNJ. Rolling friction for hard cylinder and sphere on viscoelastic solid. Eur Phys J E 2010;33:327–33.
[12] Hunter SC. The rolling contact of a rigid cylinder with a viscoelastic half space. Trans ASME E J Appl Mech 1961;28:611.
[13] Goryacheva IG. Contract problem of rolling of a viscoelastic cylinder along a base made of the same material. Prikl Mat Mekh 1973;37:925.
[14] Greenwood JA, Tabor D. The friction of hard sliders on lubricated rubber: the importance of deformation losses. Proc R Soc London Ser A 1958;71:989.
[15] Greenwood JA, Minshall H, Tabor D. Hysteresis losses in rolling and sliding friction. Proc R Soc London Ser A 1961;259:480.
[16] Tabor D. The rolling and skidding of automobile tyres. Phys Educ 1994;29:301–6.
[17] Felhos D, Xu D, Schlarb AK, Varadi K, Goda T. Viscoelastic characterization of an EPDM rubber and finite element simulation of its dry rolling friction. Express Polym Lett 2008;2(3):157–64.
[18] Carbone G, Putignano C. A novel methodology to predict sliding and rolling friction of viscoelastic materials: theory and experiments. J Mech Phys Solids 2013;61(8):1822–34.
[19] Persson BNJ. Theory of rubber friction and contact mechanics. J Chem Phys 2001;115(8):3840–61.
[20] Hooke CJ, Huang P. Elastohydrodynamic lubrication of soft viscoelastic materials in line contact. Proc Inst Mech Eng Part J: J Eng Tribol 1997;211:185.
[21] Elsharkawy AA. Visco-elastohydrodynamic lubrication of line contacts. Wear 1996;199:45–53.
[22] Persson BNJ, Scaraggi M. On the transition from boundary lubrication to hydrodynamic lubrication in soft contacts. J Phys Condens Matter 2009;21(18):185002.
[23] Persson BNJ, Scaraggi M. Lubricated sliding dynamics: flow factors and Stribeck curve. Eur Phys J E 2011;34(10):113.
[24] Scaraggi M, Carbone G, Persson BNJ, Dini D. Lubrication in soft rough contacts: a novel homogenized approach. Part I—Theory Soft Matter 2011;7(21):10395–406.
[25] Scaraggi M, Carbone G, Dini D. Lubrication in soft rough contacts: a novel homogenized approach. Part II—discussion. Soft Matter 2011;7(21):10407–16.
[26] Sivebaek IM, Samoilov VN, Persson BNJ. Velocity dependence of friction of confined hydrocarbons. Langmuir 2010;26(11):8721–8.
[27] Sivebaek IM, Samoilov VN, Persson BNJ. Squeezing molecular thin alkane lubrication films between curved solid surfaces with long-range elasticity: layering transitions and wear. J Chem Phys 2003;119(4):2314–21.
[28] Persson BNJ. Theory of friction: stress domains, relaxation, and creep. Phys Rev B 1995;51:13568.
[29] Martin A, Clain J, Buguin A, Brochard-Wyart F. Wetting transitions at soft, sliding interfaces. Phys Rev E 2002;65:031605.
[30] Schallamach A. A theory of dynamic rubber friction. Wear 1963;6(5):375–3826.
[31] Brochard-Wyart F, de Gennes PG. Naive model for stick-slip processes. Eur Phys J E 2007;23(4):439–44.
[32] Persson BNJ. Adhesion between an elastic body and a randomly rough hard surface. Eur Phys J E 2002;8:385.
[33] Persson BNJ. Contact mechanics for randomly rough surfaces. Surf Sci Rep 2006;61:201.
[34] Yang C, Persson BNJ. Contact mechanics: contact area and interfacial separation from small contact to full contact. J Phys: Condens Matter 2008 215214.
[35] Persson BNJ. Contact mechanics for layered materials with randomly rough surfaces. J Phys Condens Matter 2012;24:095008.
[36] Scaraggi M, Carbone G, Dini D. Experimental evidence of Micro-EHL lubrication in rough soft contacts. Tribol Lett 2011;43(2):169–74.
[37] Myant C, Spikes HA, Stokes JR. Influence of load and elastic properties on the rolling and sliding friction of lubricated compliant contacts. Tribol Int 2010;43:55–63.
[38] de Vicente J, Stokes JR, Spikes HA. The frictional properties of Newtonian fluids in rolling-sliding soft-EHL contact. Tribol Lett 2005;20(3–4):273–86.
[39] Christensen RM. Theory of viscoelasticity. 2nd ed.Dover Publications Inc.; 2003.